Asociación Argentina
de Mecánica Computacional

Mecánica Computacional Vol XXXVII, págs. 1597-1607 (artículo completo)
A. Cardona, L. Garelli, J.M. Gimenez, P.A. Kler, S. Márquez Damián, M.A. Storti (Eds.)
Santa Fe, 5-7 Noviembre 2019

IMPACT OF BOUNDARY CONDITIONS ON THE COMPUTATIONAL ASSESSMENT OF FRACTIONAL FLOW RESERVE

Carlos C. Bulant[b,f], **Gonzalo D. Ares**[a,f], **Cristiano G. Bezerra**[e], **Raúl A. Feijóo**[d,f], **Alejandro Clausse**[b,c], **Pedro A. Lemos**[e,f] **and Pablo J. Blanco**[d,f]

[a]*CONICET and Universidad Nacional de Mar del Plata, UNMdP, Argentina*

[b]*CONICET and Universidad Nacional del Centro, UNICEN, Argentina*

[c]*Comisión Nacional de Energía Atómica, CNEA, Argentina*

[d]*National Laboratory for Scientific Computing, LNCC/MCTIC, Petrópolis, Brazil*

[e]*Heart Institute, University of São Paulo Medical School, INCOR-FM-USP, São Paulo, Brazil*

[f]*National Institute of Science and Technology in Medicine Assisted by Scientific Computing, INCT-MACC, Brazil*

Keywords: Computational Fluid Dynamics, Coronary Circulation Model, Myocardial Ischemia.

Abstract. Coronary artery disease (CAD) may leads to myocardial ischemia, the main cause of death worldwide. Nowadays, fractional flow reserve (FFR) is considered the gold standard procedure to assess risk of myocardial ischemia in presence of CAD. The FFR index is defined as the ratio of intravascular blood pressure before and after the arterial lesion under maximal hyperemia conditions. Therefore, FFR is obtained through an invasive procedure, which requires specialized cardiologist and dedicated medical instrumentation and consequently it is expensive and not risk free.

In recent years, the computational biomechanics community has been developing tools for the FFR estimation using computational fluid dynamics (CFD) and medical image based models (hereafter FFR_{CE}), receiving increasing interest from cardiologists around the world. The implementation of these models as diagnosis tools has the potential to improve patient's experience, decrease the number of unnecessary invasive studies and reduce economic costs associated to diagnosis and treatment of CAD.

Most of past and current literature focused on proposing computational solutions for the estimation of FFR, nevertheless, they generally lack comprehensive sensitivity analyses assessing the implications of changes in the hemodynamics parameters. Here, we present an exhaustive analysis on physiologic parameters that translate into boundary conditions (BC) of the computational model. Specifically, we study the impact of the coronary flow reserve (CFR), the flow distribution in the coronary tree and the coronary steal on the FFR_{CE}. We employed a set of 24 coronary computed tomography angiography (CCTA) images to construct the patient specific arterial models and solve the full 3D CFD problem. Blood flow was modeled using the Navier-Stokes equations for rigid domains, i.e., arterial compliance was neglected. A total of 35 invasive FFR measurements are available, and those value are used as reference to assess the variations due to changes in the BC. The impact of such variations in the BC is extensively discussed.

1 INTRODUCTION

Nowadays, fractional flow reserve (FFR_{inv}) is considered the gold standard technique to assess risk of myocardial ischemia in the presence of coronary artery disease (CAD) (Tonino et al., 2009). It is calculated as the ratio of post- and pre-stenotic blood pressure measurements under hyperemic conditions. In clinical protocols, $\text{FFR}_{\text{inv}} \leq 0.8$ indicates that the patient is at risk of suffering myocardial ischemia due to the functional severity of the stenosis.

In recent years, the scientific community specialized in computational hemodynamics incurred in the estimation of FFR_{inv} through computer simulations, here after FFR_{CE}. From a general perspective, patient-specific hemodynamic simulations rely on the definition of two fundamental issues: (i) computational domains and (ii) boundary conditions (BC). Vascular geometries can be obtained using a variety of imaging techniques: coronary computed tomography angiography (CCTA) Choi et al. (2015); Rikhtegar et al. (2012); Taylor et al. (2013) or angiograms (AX), which can be utilized alone Campbell et al. (2013); Morris et al. (2015), or in combination with either intravascular ultrasound (IVUS) Chatzizisis et al. (2008); Koskinas et al. (2010); Stone et al. (2003); Siogkas et al. (2013) or optical coherence tomography (OCT) Ellwein et al. (2011); Ha et al. (2016). In turn, the definition of boundary conditions requires knowledge of global and local hemodynamic information, i.e. systemic pressure, total coronary blood flow and blood flow distribution.

Generally, the literature addressing the computational estimation of FFR_{inv} concentrates on comparing a given proposed methodology to the invasive measurements (**?**). Hence, the impact of model parameters (implied in the definition of BCs) on the simulation outcomes is generally overlooked. Nevertheless, studying such effect is crucial to understand the estimation errors and improve the methodological procedures. Empirical analyses require the realization of several computer simulations varying the BC.

In this work, images from CCTA are used to obtain patient-specific models of the coronary vasculature, and the impact on the computation of the FFR_{CE} of several boundary conditions is assessed.

2 MATERIALS AND METHODS

The computational workflow followed in this study is depicted in Figure 1 and consists of 5 main stages: (1) *Input of medical data*, which includes the CCTA image and patient clinical status, see Section 2.1. (2) *Image processing*, consists of the image segmentation pipeline, see Section 2.2, which outputs a raw surface mesh of the coronary arterial lumen; this stage also accounts for the segmentation/estimation of other anatomical structures such us myocardial surface and volume. (3) *Arterial network modeling*, post-processing of the raw surface results in a mesh fit for CFD simulations and a corresponding representation of vessels through their centerlines, whose processing includes arterial labeling and bifurcations detection, see Section 2.3. (4) *Scenario preset and simulation*, various hemodynamics scenarios are preset through different boundary conditions, each of one represent a computational simulation, see Section 2.5. (5) *Post-processing and data analysis*, the FFR_{CE} is computed from the simulation outcome, see Section 2.6, and statistical analysis over such data is performed.

All image processing stages, as well as meshing and centerline processing, are performed using VMTK web (2015), ImageLab Hadlich et al. (2012) and HeMoLab Larrabide et al. (2012) software.

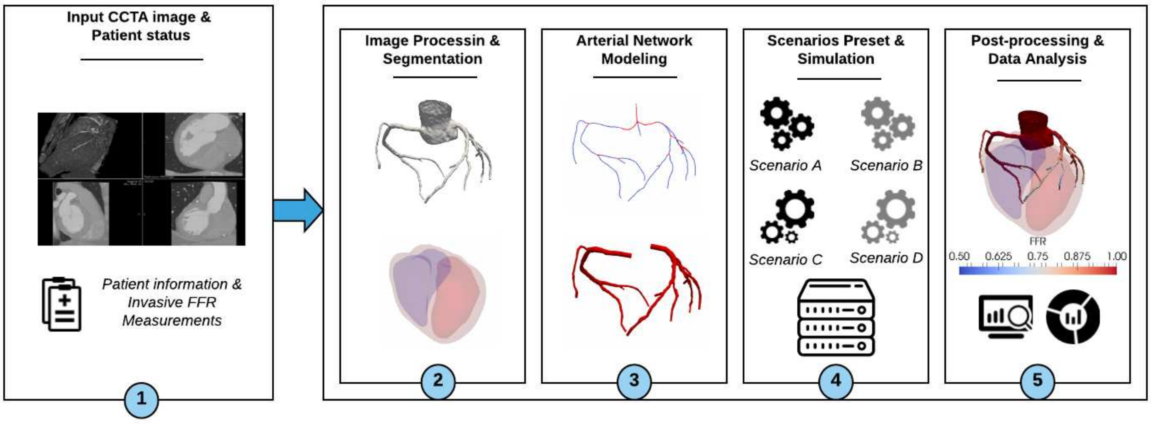

Figure 1: Illustration of the computational workflow.

Baseline clinical characteristic	**Patient sample** $(n = 24)$
Age, yrs	61±9
Male	21 (87)
BMI, kg/m2	28±3
Weight, Kg	85±15
Height, cm	174±10
HR, bpm	70±8
SP, mmHg	113±13
DP, mmHg	68±10
MP, mmHg	84±10
Circulation Dominance	
Right	22 (92)
Left	1 (4)
Co	1 (4)

Table 1: Summary of patient data, the mean ± SD, or n (%), are reported. Body mass index (BMI), heart rate (HR), diastolic, systolic and mean pressures (DP, SP and MP).

Baseline lesion characteristic	**Vessel sample** $(n = 35)$
LAD	21 (60)
LCX	6 (17)
RI	1 (3)
OM	1 (3)
RCA	6 (17)
FFR_{inv}	0.88±0.08 (0.71, 0.99)

Table 2: Summary of lesions, the mean ± SD (min, max), or n (%), are reported.

	Circ. Dominance	**LAD**	**LCx**	**RCA**	**RI**
RI not present	**Right**	60	22	18	0
	Left	60	30	10	0
	Co	60	24	16	0
RI present	**Right**	57	10	18	15
	Left	60	15	10	15
	Co	59	10	16	15

Table 3: Percentage of the Q_T at the inlet of each major artery.

2.1 Study sample

The sample is constituted by patients with suspected chronic coronary disease who underwent multimodal evaluation with CCTA and a posterior FFR_{inv}. The study protocol was approved by the ethics committees of the Heart Institute (University of São Paulo) and the Sírio-Libanês Hospital, both in São Paulo, Brazil. Overall, 35 vessels of 24 patients were assessed using FFR_{inv}. Baseline clinical and lesions characteristics are outlined in Tables 1 and 2.

Imaging data were acquired following standardized image acquisition protocols, i.e. using ECG-triggered imaging at 75% of the cardiac cycle (late diastole) and ensuring patient heart rate lower than 65 bpm. Data processing and analysis were performed retrospectively and described in the following sections.

2.2 Image processing

Segmentation of CCTA images is achieved using the methodology detailed in Bulant et al. (2017). Briefly, the pipeline starts with the extraction of a region of interest on top of which curvature anisotropic filtering Whitaker and Xue (2001) is applied for noisy images. Segmentation is performed using a level-set method, initialized using a colliding front algorithm Antiga et al. (2008). The segmented lumen is defined using a marching cubes method Lorensen and Cline (1987). This procedure results in a triangulated raw surface of the coronary tree. Additionally, the myocardial volume is estimated from the image following the procedure explained in Bulant et al. (2017).

2.3 Computational model generation

The coarse mesh from Section 2.2 is further processed to obtain the computational mesh suitable for the CFD simulations. Surface mesh processing consists in (a) smoothing with a Laplacian algorithm with no shrinking restriction, (b) incorporation of tube extension at inlet/outlets and (c) adaptive refinement as a function of vessel cross-sectional radius. Finally, a tetrahedral volume mesh is constructed for the CFD simulations. An expanded explanation of the mesh processing pipelines used to obtained the CFD meshes can be found in Bulant (2017).

The vessel cross-sectional radius is given by the arterial tree centerline, which is obtained following Antiga et al. (2003). The centerline is then processed to account for a bifurcation mask that defines the arterial ostium of each artery, and the anatomical name of each artery is assigned as labels, see Bulant et al. (2017) for details.

2.4 Computational fluid dynamics

Blood flow was modeled using the Navier-Stokes equations in rigid domains, i.e., arterial compliance was neglected. Then, the computational solution consists of finding the velocity ($\mathbf{v}$) and pressure p fields of the fluid. Parameters are: the blood density (ρ); the blood viscosity (μ); the blood pressure at the inlet of the arterial tree (P_p, i.e. aortic pressure); a reference value for the blood pressure at terminal outlets (P_{ref}, i.e. venous pressure); the total coronary blood flow, Q_T; and the resistances at each outlet R_i. In this work, two different criteria for defining the BCs are tested, which define the resistances at terminals. Methodology (i) makes use of traditional resistive elements, whose values R_i are estimated using a proximal Murray's law approach, see section 2.4.1. Methodology (ii) modifies the values of resistances R_i by a factor α to enforce an exact Q_T. Both methods are detailed in Bulant (2017). Hereafter, we refer to the resistive BC methodology as RBC^R and $\text{RBC}^{R\alpha}$, respectively. Steady-state simulations are executed using constant values for the aforementioned parameters.

2.4.1 Model and patient specific parameters

In this work, the blood density and viscosity are the same for all patients, $\rho = 1.05$ g/cm^3, $\mu = 0.04$ P. The mean pressure at the root of the coronary arterial tree (P_p) is estimated for each patient. Given noninvasive measurements of systolic (SP) and diastolic (DP) pressures at rest, the P_p at hyperemia is given by $P_p = \text{MP} + \Delta$. Where $\text{MP} = (2\text{DP} + \text{SP})/3$ is the mean arterial pressure estimation and Δ is the effect of intra-coronary ($\Delta = -3.8$) or intra-venous ($\Delta = -4.4$) administration of adenosine, as reported in Bulant (2017). For each patient in the sample, it is known which kind of administration was used.

In this work, the resting coronary blood flow (RCBF) is estimated from non-invasive patient data in two different ways. The RCBF^m, uses the formula proposed by Choy and Kassab (2008), which relates flow to myocardial mass, through

$$\text{RCBF}^m = 0.71 \times m^{3/4}, \tag{1}$$

where m is the myocardial mass, in grams, and the flow is given in ml/s. Taylor et al. (2013) yields an estimate of patient-specific RCBF using (1). In turn, we call RCBF^n to the resting coronary blood flow estimated as 4.5% of the cardiac output (CO) Guyton and Hall (2006),

$$
\begin{aligned}
\text{RCBF}^n =& 0.045 \times \text{CO}, && (2)\\
\text{CO} =& \frac{\text{HR} \times \text{SV}}{1000}, && (3)\\
\text{SV} =& (0.49 \times \text{PP} + 0.30 \times \text{A} + 7.11)\\
& \times (0.013 \times \text{W} - 0.007 \times \text{A} - 0.004 \times \text{HR} + 1.307), && (4)
\end{aligned}
$$

where HR is the heart rate (in beats/s), SV is the stroke volume (in ml/beat), which is estimated following (de Simone et al., 1999) from the pulse pressure[1] (PP, in mmHg), the age of the patient (A, in years) and its weight (W, in Kg).

For the study sample, the estimated RCBF^n is 4.19 ± 0.67 ml/s, which is in the physiological range (4.5 ± 1.37 ml/min) reported by Sakamoto et al. (2013). In contrast, RCBF^m results in 0.68 ± 0.13 ml/s, which is significantly lower than physiological data.

Coronary flow reserve (CFR) is defined as the ratio between hyperemic and resting blood flow. Therefore, the hyperemic flow is CBF $=$ CFR $\times$ RCBF. In non-ischemic human coronary arteries, CFR mean value is $\sim$ 2.6 (Johnson et al., 2012). Previous works that aim to estimate FFR computationally Koo et al. (2011); Min et al. (2011); Gaur et al. (2013); Zhang et al. (2016), model hyperemia by reducing terminal resistances by a factor of 4.5, based on the seminal findings by Wilson et al Wilson et al. (1990). Hence, we test both values of CFR=$\{2.6, 4.5\}$.

Terminal resistances for a given arterial tree are estimated using a variation of Murray's law Murray (1926), which considers the arterial cross sectional radius at the ostiums instead of the outlets and ensures that the CBF is distributed according to Table 3 for the inlets of the major coronary arteries. The Murray exponent is set to $\gamma = 2.66$ motivated by allometric laws relating flow to volume of tissue Blanco et al. (2013). Details of the algorithm used to estimate terminal resistances based on inflow, P_p, ostium radius and a reference venous pressure ($P_{\text{ref}} = 10$ mmHg) are described in Bulant (2017). For the study sample, the average resting flow rates at the inlet of the LAD, LCx and RCA arteries are 3.38 ± 1.18, 1.40 ± 0.85 and 0.85 ± 0.33 ml/s.

2.5 Simulation scenarios

We propose the use of 4 scenarios, each one designed to assess the effect of a specific BC criterion. To such end, we define the **SA** scenario as baseline and define the others as a variation of one specific BC criterion.

- **SA**: Uses the RBC$^{R\alpha}$ as resistive boundary condition, the resting coronary blood flow is estimated using RCBF^n and the value of CFR is set to 2.6.
- **SB**: Uses the RBC$^{R\alpha}$ as resistive boundary condition, the resting coronary blood flow is estimated using RCBF^n and the value of CFR is set to 4.5.
- **SC**: Uses the RBC^{R} as resistive boundary condition, the resting coronary blood flow is estimated using RCBF^n and the value of CFR is set to 2.6.
- **SD**: Uses the RBC$^{R\alpha}$ as resistive boundary condition, the resting coronary blood flow is estimated using RCBF^m and the value of CFR is set to 2.6.

---

[1] Systolic blood pressure (SBP) minus diastolic blood pressure (DBP).

2.6 Simulation post-processing

After the simulation is performed, approximate solutions for the velocity ($\mathbf{v}$) and pressure (p) fields are available at each node in the computational mesh. Estimation of FFR$_{\mathrm{CE}}$ field requires the definition of a proximal pressure P_a, which is calculated as the spatial average at the inlet region of approximately 2 mm length. Such region is manually defined using points of the centerline, which are used to clip the tetrahedral mesh. Then, a new field containing the FFR at each computational node is calculated as

$$\mathrm{FFR}(\mathbf{x}) = \frac{p(\mathbf{x})}{P_a}, \tag{5}$$

Then, the final FFR$_{\mathrm{CE}}$ value is estimated as the average of the FFR$(\mathbf{x})$ at a distal region of approximately 2 mm length, manually defined. Such region is identified as Ω_{FFR}, and its definition is guided by AX images showing the location of the invasive pressure wire during the clinical FFR procedure. We define such a value as Computational Estimation of the Fractional Flow Reserve (FFR$_{\mathrm{CE}}$).

3 RESULTS

Figure 2 presents correlation and Bland-Altman plots for all four scenarios and Table 4 presents the diagnostic performance summary. The sample consists in 24 patients with 35 interrogated vessels and a 25.7% prevalence (FFR$_{\mathrm{inv}} \leq 0.8$).

It is worth noting the overestimation in scenario **SD**, resulting in ${\mathrm{FFR}_{\mathrm{CE}}}^{\mathrm{SD}} \geq \mathrm{FFR}_{\mathrm{inv}}$ for all measurements. As a consequence, the SEN $= 0$, SPE $= 1$ and PPV $=$ NAN. Such results are caused by lower values of resting coronary blood flow and, therefore, of hyperemic blood flow. Specifically, RCBF^m represents $16.4 \pm 3.4\%$ of RCBF^m, and since the CFR is set to 2.6 for **SD**, the flow rate is not enough to produce significant pressure drops.

On the contrary, **SB** scenario is characterized by the largest hyperemic blood flow and consequently the largest pressure drops. The combination of RCBF^n and a CFR=4.5 results in underestimation of FFR$_{\mathrm{CE}}$ values for several measurements. Specifically, only in 8 out of 35 interrogated arteries, the ${\mathrm{FFR}_{\mathrm{CE}}}^{\mathrm{SB}} \geq \mathrm{FFR}_{\mathrm{inv}}$ and from those, 5 are RCA arteries and the other three are LAD arteries. This is a clear example of patients that may have smaller physiological values of CFR. In fact, according to Johnson et al. (2012) the CFR ranges in (1, 6) with mean 2.57 ± 0.61 for non-ischemic hearts. Other explanation for the case of RCA arteries may stem from an overestimation of the RCBF distribution for the RCA inlet.

Regarding scenario **SC**, although it achieved the lowest error and dispersion in the Bland-Altman analysis (0.01±0.09) and the best linear regression coefficients, it falls short characterizing the true positive rate or sensitivity (SEN=0.44).

Despite the proposed scenario **SA** does not reach highest predictive scores than the other scenarios in each index, it achieves a good overall balance of predictive scores.

In terms of flow rates, Table 5 presents the mean and standard deviations of the blood flow at the inlet of the coronary sub-tree that contains the interrogated artery (SFST) and the flow rate at the location of FFR$_{\mathrm{CE}}$ measurement (Ω_{FFR}). Such values are the result of the simulation, and may not be strictly related to the BCs. Taking into consideration that RBC$^{R\alpha}$ enforces the desired flow adapting the resistances, it is remarkable that RBC^{R} consistently results in smaller SFST values than its counterpart, comparing **SC** and **SA**. Specifically, the value of SFST from scenario **SC** represents the 76±12 % of the SFST value from **SA**. Which means that taking into account the resistance of the large arteries to better characterize the resistive boundary condition to achieve a given flow rate is essential.

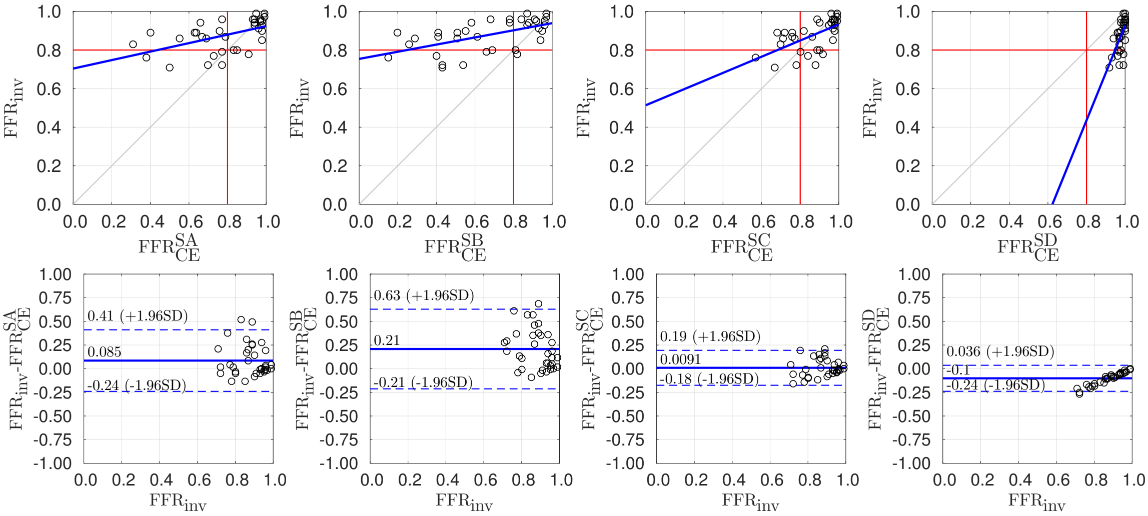

Figure 2: Scatter and Bland-Altman plots comparing FFR_{inv} with FFR_{CE} for each scenario. From top to bottom, scenarios SA, SB, SC and SD.

Comparison	AUC	ACC	SEN	SPE	PPV	NPV	$r^{\dagger}$	BA	α	β
FFR_{inv} vs $FFR_{CE}{}^{SA}$	0.70	0.60	0.67	0.58	0.35	0.83	0.52	0.09 ± 0.17 ‡	0.22	0.70
FFR_{inv} vs $FFR_{CE}{}^{SB}$	0.72	0.57	**0.78**	0.50	0.35	**0.87**	0.57	0.21 ± 0.21	0.19	0.75
FFR_{inv} vs $FFR_{CE}{}^{SC}$	0.74	0.66	0.44	0.73	**0.36**	0.79	0.60	**0.01 ± 0.09** ‡	**0.42**	**0.51**
FFR_{inv} vs $FFR_{CE}{}^{SD}$	**0.79**	**0.74**	0.00	**1.00**	NaN	0.74	**0.64**	-0.10 ± 0.07	2.46	-1.53

Table 4: Predictive capabilities of each scenario. The prevalence of FFR_{inv} in the $n = 35$ measurements is 25.7%. Columns denote the area under the ROC curve (AUC), accuracy (ACC), sensitivity (SEN), specificity (SPE), positive predictive value (PPV), negative predictive value (NPV), Pearson's correlation coefficient (r, † stands for $p < 0.01$), Bland-Altman mean ± standard deviation (‡ indicates $p > 0.01$), and linear regression coefficients $FFR_{inv} = \alpha FFR_{CE} + \beta$. For each column, the best scenario performance is highlighted in bold font.

On the other hand, comparing **SA** and **SB** yields that SFST is 1.73 ± 0.00 times larger in **SB**. Which was expected because both enforce the flow using $RBC^{R\alpha}$ (1.73 is the ratio between CFR values 4.5 and 2.6). Nevertheless, comparing the flow at Ω_{FFR}, the simulations resulted in 1.5 ± 0.33 (range $[0.97, 2.21]$) times larger flow in the **SB** compared to the corresponding **SA**. Such result is explained by the coronary steal phenomenon and can only be achieved using resistive BC, either $RBC^{R\alpha}$ or RBC^{R}. Flow rate per each arterial segment depends upon the terminal resistance and the resistance of the major vessels. Changing the terminal resistance changes the ratio of terminal-vessel resistance, and therefore the flow distribution.

4 DISCUSSIONS

In this work we have evaluated the combined effect of modifying the type of boundary condition as well as the CFR which determines the hyperemic coronary blood flow.

The definition of boundary condition is crucial for the proper estimation of FFR_{CE}. In fact, it directly affects the flow through the lesion, which in turn determines the pressure drop and the FFR estimation.

Three criteria in the definition of BCs can counteract the definition of the through-lesion blood flow. These are (i) the definition of the RCBF, (ii) the definition of the CFR induced by

Comparison	SFST	Ω_{FFR} Flow
$\mathrm{FFR_{CE}}^{\mathrm{SA}}$	7.56 ± 2.89	1.5370 ± 0.6509
$\mathrm{FFR_{CE}}^{\mathrm{SB}}$	13.09 ± 5.00	2.2576 ± 0.9609
$\mathrm{FFR_{CE}}^{\mathrm{SC}}$	5.53 ± 2.01	1.2160 ± 0.5320
$\mathrm{FFR_{CE}}^{\mathrm{SD}}$	1.26 ± 0.52	0.2867 ± 0.1730

Table 5: Simulated blood flow at the inlet of the coronary sub-tree that contains the interrogated artery (called SFST) and flow rate at the location of $\mathrm{FFR_{CE}}$ measurement. The mean and standard deviation for each scenario is presented, values are in cm^3/s.

hyperemia, and the (iii) the regional blood flow distribution.

The first two shift the pressure level along the entire coronary vasculature, and therefore affect the coronary hemodynamics at a global level. We have assumed a one-fits-all approach for the definition of the CFR, which might not be a realistic physiological assumption. In turn, the definition of terminal resistances has a more pronounced impact in the regional blood flow distribution once the RCBF has been established. Therefore, the use of passive resistive elements, in contrast to active elements that are adapted to guarantee a certain blood flow through major branches, triggers different levels of coronary steal, leading to dissimilar blood flows through the lesions and consequently to different values of $\mathrm{FFR_{CE}}$.

Specifically, we have shown that BCs reported in the literature based on myocardial mass render unsatisfactory results, in contrast to BCs relying on CO estimates as proposed in this work (compare scenarios **SA** and **SD**). Moreover, since the CO can be measured at a patient-specific level non-invasively, the problem turns out to be the definition of the fraction of the CO which is diverted to the coronary network (in this case 4.5%).

From the different studied scenarios, we have shown that not only the definition of the CFR and the criteria to define RCBF are of primary importance, but also the nature of resistive terminal elements, passive (defined a priori) in contrast to active (adapted to enforce a given blood flow rate), have a significant impact in the estimation of FFR.

Based on the experience gathered in this work, higher values of CFR produce the shift of the entire sample towards smaller values of $\mathrm{FFR_{CE}}$ (comparing scenarios **SA** and **SB**). This is not enough to improve the correlation coefficients neither to improve the results reported in the Bland-Altman plots. Further improvements can be gained from assuming differential hyperemic conditions for the different myocardial territories. In fact, for a given CFR the results turned out to be sensitive to the type of resistive element to model peripheral vasculature (compare scenarios **SA** and **SC**).

Even if much still remains to be studied, the present work allows us to conclude that the improvement of computational approaches for a more robust estimation of FFR should stem from studies analyzing, in a definite and unambiguous manner, the sensitivity and impact of modeling assumptions into the overall prediction indexes.

ACKNOWLEDGEMENTS

This work was partially supported by Brazilian agencies CNPq and FAPERJ; NVIDIA Hardware Grant. The support of these agencies is gratefully acknowledged.

REFERENCES

The Vascular Modeling Toolkit website. 2015.

Antiga L., Ene-Iordache B., and Remuzzi A. Computational geometry for patient-specific reconstruction and meshing of blood vessels from MR and CT angiography. *IEEE Transactions on Medical Imaging*, 22(5):674–684, 2003.

Antiga L., Piccinelli M., Botti L., Ene-Iordache B., Remuzzi A., and Steinman D.A. An image-based modeling framework for patient-specific computational hemodynamics. *Medical & Biological Engineering & Computing*, 46(11):1097–1112, 2008. ISSN 0140-0118, 1741-0444.

Blanco P., Queiroz R., and Feijóo R. A computational approach to generate concurrent arterial networks in vascular territories. *International Journal for Numerical Methods in Biomedical Engineering*, 29:601–614, 2013.

Bulant C. *Computational models for the geometric and functional assessment of the coronary circulation.* Ph.D. thesis, National Laboratory for Scientific Computing, 2017.

Bulant C.A., Blanco P.J., Lima T.P., Assunção A., Liberato G., Parga J.R., Ávila L.F.R., Pereira A.C., Feijóo R.A., and Lemos P.A. A computational framework to characterize and compare the geometry of coronary networks. *International Journal for Numerical Methods in Biomedical Engineering*, 33(3):e02800, 2017.

Campbell I., Timmins L., Giddensa D., Virmanic R., Veneziani A., Rab S.T., Samady H., McDaniel M., Finn A., Taylor W., and Oshinski J. Computational fluid dynamics simulations of hemodynamics in plaque erosion. *Cardiovascular Engineering and Technology*, 4:464–473, 2013.

Chatzizisis Y., Jonas M., Coskun A., Beigel R., Stone B., Maynard C., Gerrity R., Daley W., C.Rogers, Edelman E., Feldman C., and Stone P. Prediction of the localization of high-risk coronary atherosclerotic plaques on the basis of low endothelial shear stress. An intravascular ultrasound and histopathology natural history study. *Circulation*, 117:993–1002, 2008.

Choi G., Lee J., Kim H.J., Park J.B., Sankaran S., Otake H., Doh J.H., Nam C.W., Shin E.S., Taylor C., and Koo B.K. Coronary artery axial plaque stress and its relationship with lesion geometry. Application of computational fluid dynamics to coronary CT angiography. *Journal of the American College of Cardiology: Cardiovascular Imaging*, 8:1156–1166, 2015.

Choy J.S. and Kassab G.S. Scaling of myocardial mass to flow and morphometry of coronary arteries. *Journal of Applied Physiology*, 104(5):1281–1286, 2008.

de Simone G., Roman M.J., Koren M.J., Mensah G.A., Ganau A., and Devereux R.B. Stroke volume/pulse pressure ratio and cardiovascular risk in arterial hypertension. *Hypertension*, 33(3):800–805, 1999.

Ellwein L., Otake H., Gundert T., Koo B.K., Shinke T., Honda Y., Shite J., and Jr. J.L. Optical coherence tomography for patient-specific 3D artery reconstruction and evaluation of wall shear stress in a left circumflex coronary artery. *Cardiovascular Engineering and Technology*, 2:212–227, 2011.

Gaur S., Achenbach S., Leipsic J., Mauri L., Bezerra H.G., Jensen J.M., Bøtker H.E., Lassen J.F., and Nørgaard B.L. Rationale and design of the HeartFlowNXT (HeartFlow analysis of coronary blood flow using CT angiography: NeXt sTeps) study. *Journal of Cardiovascular Computed Tomography*, 7(5):279–288, 2013.

Guyton A.C. and Hall J.E. *Textbook of medical physiology*. Elsevier Saunders, Philadelphia, 11th ed edition, 2006.

Ha J., Kim J.S., Lim J., Kim G., Lee S., Lee J.S., Shin D.H., Kim B.K., Ko Y.G., Choi D., and others. Assessing Computational Fractional Flow Reserve From Optical Coherence Tomography in Patients With Intermediate Coronary Stenosis in the Left Anterior Descending Artery. *Circulation: Cardiovascular Interventions*, 9(8):e003613, 2016.

Hadlich M.S., Oliveira G.M.M., Feijóo R.A., Azevedo C.F., Tura R., Ziemer P.G.P., Blanco

P.J., Pina G., and Meira M. Free and Open-Source Software Application for the Evaluation of Coronary Computed Tomography Angiography Images. *Arq Bras Cardiol.*, page 8, 2012.

Johnson N.P., Kirkeeide R.L., and Gould K.L. Is Discordance of Coronary Flow Reserve and Fractional Flow Reserve Due to Methodology or Clinically Relevant Coronary Pathophysiology? *JACC: Cardiovascular Imaging*, 5(2):193–202, 2012.

Koo B., Erglis A., Doh J., Daniels D., Jegere S., Kim H., Dunning A., DeFrance T., Lansky A., Leipsic J., and Min J. Diagnosis of ischemia-causing coronary stenoses by noninvasive fractional flow reserve computed from coronary computed tomographic angiograms. results from the prospective multicenter DISCOVER-FLOW (diagnosis of ischemia-causing stenoses obtained via noninvasive fractional flow reserve) study. *J Am Coll Cardiol*, 58(19):1989–97, 2011.

Koskinas K., Feldman C., Chatzizisis Y., Coskun A., Jonas M., C.Maynard, Baker A., M.I. Papafaklis E.E., and Stone P. Natural history of experimental coronary atherosclerosis and vascular remodeling in relation to endothelial shear stress. A serial, in vivo intravascular ultrasound study. *Circulation*, 121:2092–2101, 2010.

Larrabide I., Blanco P., Urquiza S., Dari E., Vénere M., de Souza e Silva N., and Feijóo R. Hemolab hemodynamics modelling laboratory: An application for modelling the human cardiovascular system. *Computers in Biology and Medicine*, 42:993–1004, 2012.

Lorensen W.E. and Cline H.E. Marching cubes: A high resolution 3d surface construction algorithm. *Computer Graphics*, 21(4):163–169, 1987.

Min J.K., Berman D.S., Budoff M.J., Jaffer F.A., Leipsic J., Leon M.B., Mancini G.J., Mauri L., Schwartz R.S., and Shaw L.J. Rationale and design of the DeFACTO (Determination of Fractional Flow Reserve by Anatomic Computed Tomographic AngiOgraphy) study. *Journal of Cardiovascular Computed Tomography*, 5(5):301–309, 2011.

Morris P.D., van de Vosse F.N., Lawford P.V., Hose D.R., and Gunn J.P. “Virtual” (Computed) Fractional Flow Reserve. *JACC: Cardiovascular Interventions*, 8(8):1009–1017, 2015.

Murray C.D. The physiological principle of minimum work: I. The vascular system and the cost of blood volume. *Proceedings of the National Academy of Sciences of the United States of America*, 12(3):207, 1926.

Rikhtegar F., Knight J., Olgac U., Saur S., Poulikakos D., Jr. W.M., Cattin P., Alkadhi H., and Kurtcuoglu V. Choosing the optimal wall shear parameter for the prediction of plaque location - A patient-specific computational study in human left coronary arteries. *Atherosclerosis*, 221:432–437, 2012.

Sakamoto S., Takahashi S., Coskun A.U., Papafaklis M.I., Takahashi A., Saito S., Stone P.H., and Feldman C.L. Relation of Distribution of Coronary Blood Flow Volume to Coronary Artery Dominance. *The American Journal of Cardiology*, 111(10):1420–1424, 2013.

Siogkas P.K., Papafaklis M.I., Sakellarios A.I., Stefanou K.A., Bourantas C.V., Athanasiou L.M., Bellos C.V., Exarchos T.P., Naka K.K., Michalis L.K., and others. Computational assessment of the fractional flow reserve from intravascular ultrasound and coronary angiography data: A pilot study. In *Engineering in Medicine and Biology Society (EMBC), 2013 35th Annual International Conference of the IEEE*, pages 3885–3888. IEEE, 2013.

Stone P., Coskun A., Kinlay S., Clark M., Sonka M., Wahle A., Ilegbusi O., Yeghiazarians Y., Popma J., Orav J., Kuntz R., and Feldman C. Effect of endothelial shear stress on the progression of coronary artery disease, vascular remodeling, and in-stent restenosis in humans. In vivo 6-month follow-up study. *Circulation*, 108:438–444, 2003.

Taylor C.A., Fonte T.A., and Min J.K. Computational Fluid Dynamics Applied to Cardiac Computed Tomography for Noninvasive Quantification of Fractional Flow Reserve. *Journal* *of the American College of Cardiology*, 61(22):2233–2241, 2013.

Tonino P.A.L., De Bruyne B., Pijls N.H.J., Siebert U., Ikeno F., van' t Veer M., Klauss V., Manoharan G., Engstrøm T., Oldroyd K.G., Ver Lee P.N., MacCarthy P.A., Fearon W.F., and FAME Study Investigators. Fractional flow reserve versus angiography for guiding percutaneous coronary intervention. *The New England journal of medicine*, 360(3):213–224, 2009.

Whitaker R.T. and Xue X. Variable-conductance, level-set curvature for image denoising. In *Image Processing, 2001. Proceedings. 2001 International Conference on*, volume 3, pages 142–145. IEEE, 2001.

Wilson R.F., Wyche K., Christensen B.V., Zimmer S., and Laxson D.D. Effects of adenosine on human coronary arterial circulation. *Circulation*, 82(5):1595–1606, 1990.

Zhang J.M., Zhong L., Luo T., Lomarda A.M., Huo Y., Yap J., Lim S.T., Tan R.S., Wong A.S.L., Tan J.W.C., Yeo K.K., Fam J.M., Keng F.Y.J., Wan M., Su B., Zhao X., Allen J.C., Kassab G.S., Chua T.S.J., and Tan S.Y. Simplified Models of Non-Invasive Fractional Flow Reserve Based on CT Images. *PLOS ONE*, 11(5):e0153070, 2016.